Journal of Alloys and Compounds 653 (2015) 54–60

Contents lists available at ScienceDirect

Journal of Alloys and Compounds

journal homepage: http://www.elsevier.com/locate/jalcom

Effect of processing routes on the synthesis and properties of Zn_4Sb_3 thermoelectric alloy

A. Castellero [a, *], C. Fanciulli [b], R. Carlini [c, d], G. Fiore [a], P. Mele [e], F. Passaretti [b], M. Baricco [a]

[a] Department of Chemistry and NIS, University of Turin, Turin, Italy
[b] CNR – Istituto per l'Energetica e le Interfasi, Lecco, Italy
[c] Chemistry and Industrial Chemistry Department, University of Genoa, Genoa, Italy
[d] INSTM – Interuniversitary Consortium of Science and Technology of Materials, UoR Genoa, Italy
[e] College of Design and Manufacturing Technology, Muroran Institute of Technology, Muroran, Hokkaido, Japan

ARTICLE INFO

Article history:
Received 28 July 2015
Received in revised form
28 August 2015
Accepted 29 August 2015
Available online 3 September 2015

Keywords:
Intermetallics
Rapid-solidification
Sintering
Microstructure
Thermoelectric
Mechanical properties

ABSTRACT

In this work, sintering of Zn_4Sb_3 was performed by open die pressing at 558 K, investigating the role of different starting materials (powders obtained from slowly cooled master alloy ingots or rapidly solidified ribbons) on microstructure, phase stability, thermoelectric properties and mechanical properties.

With respect to the master alloy, sintered samples show lower porosity, a slight decrease in Zn content and a partial decomposition of Zn_4Sb_3 into ZnSb and Zn. Sintering of ground rapidly solidified ribbons further reduces porosity and partially inhibits the decomposition of Zn_4Sb_3.

As sintered samples show a temperature behaviour of the Seebeck coefficient that is intermediate between those of Zn_4Sb_3 and ZnSb. Thermal cycling between 300 K and 700 K favours the homogenization of the microstructure, due to the recombination of ZnSb and Zn into Zn_4Sb_3, leading to a Seebeck coefficient typical of Zn_4Sb_3 single phase. The phase evolution observed upon sintering and thermal cycling is described in terms of competing reactions ruled by thermodynamics and kinetics, and the different behaviour of the samples is explained by the different free energy level of the starting materials.

All samples show a brittle behaviour upon stress-strain compressive test and microindentation measurements. A remarkable increase of the fracture strength is observed as the porosity decreases, whereas microhardness values are similar for all samples (220–240 HVN). For the sintered samples, values of the indentation fracture toughness (0.8–0.9 MPa $m^{1/2}$) are estimated from the length of Palmqvist-type radial cracks.

© 2015 Elsevier B.V. All rights reserved.

1. Introduction

Thermoelectric materials for waste heat recovery require high figure of merit (ZT), reliable mechanical properties, chemical and structural stability. Furthermore, the use of materials based on abundant and non-toxic elements is crucial in view of a wide spread of thermoelectric technology [1].

Zn_4Sb_3 represents a promising thermoelectric material for the intermediate temperature range (450–700 K) as a consequence of the phonon glass-type and electron crystal-type behaviour and because of the absence of rare and toxic elements such as Te and Pb [2,3]. From the thermoelectric point of view, the rhombohedral Zn_4Sb_3 phase is the most relevant one [3]. According to the Zn–Sb binary phase diagram [4,5], the rhombohedral Zn_4Sb_3 phase is stable between 253–263 K and 764–767 K. However, several authors reported evidences about the instability of Zn_4Sb_3 below 764–767 K, with consequent deterioration of the thermoelectric properties [4,6–8].

Caillat et al. [6] reported that Zn_4Sb_3 is stable only up to 670 K in argon atmosphere and 520 K in dynamic vacuum. Subsequently, Mozharivskyj et al. [4] showed by high temperature X-ray powder diffraction measurements in dynamic vacuum that Zn_4Sb_3 starts to lose Zn at 473 K and to decompose into ZnSb and Zn at 623 K.

Thermal stability of Zn_4Sb_3 is also influenced by sample preparation. For instance, after thermal cycling, samples prepared by zone melting retain about 91 wt.% of the rhombohedral phase, whereas samples obtained by water quenching show a drop of the amount down to about 42 wt.% [8]. As suggested by Iversen [3], the sample prepared by zone melting likely presents a low fraction of defects in the crystalline lattice, because crystal growth occurs in

* Corresponding author.
E-mail address: alberto.castellero@unito.it (A. Castellero).

http://dx.doi.org/10.1016/j.jallcom.2015.08.251
0925-8388/© 2015 Elsevier B.V. All rights reserved.

conditions close to the equilibrium. Conversely, a quenched sample is likely highly defective as a consequence of the non-equilibrium synthesis conditions. Thus, a high density of defects improves atomic mobility, favouring the loss of Zn.

Concerning mechanical properties, Ueno et al. [9] highlighted that a significant limit of Zn_4Sb_3 for application in thermoelectric generators (TEGs) is its brittle behaviour. It was estimated that thermal stress can exceed fracture strength, leading to fracture of the thermoelectric leg in the module [9]. Zn_4Sb_3 samples prepared from the melt by free cooling [6] or Bridgman method [10] undergo to a solid state reaction at about 767 K [4,5] and develop microcracks because of volumetric changes, due to the different thermal expansion coefficients, during the phase transformation [6]. Therefore, the typical preparation of bulk and dense Zn_4Sb_3 is based on powder metallurgy processing, where compaction of single phase powders is usually performed by hot pressing [6,9,11–13] or spark plasma sintering (SPS) [14,15]. In the literature, different approaches were attempted in order to improve mechanical properties (e.g. fracture toughness and fracture strength) of Zn_4Sb_3 [11–15].

A first possible approach is to optimize the mechanical properties of the single phase material by tuning the particles size of the powders used for compaction [13]. An increase of fracture toughness was observed by decreasing the average particle size. No correlation between thermoelectric properties and particles size was established. However, samples prepared with smaller particles showed a higher oxygen contamination after crushing and sieving, due to the larger surface area exposed to the atmosphere, and, consequently, a decrease of electrical conductivity.

A step forward consists in refining the microstructure of the crystalline Zn_4Sb_3 single phase by non-equilibrium techniques, such as rapid solidification [15]. In this case, a submicrometric multi-phase microstructure can be obtained after quenching that develops into a submicrometric single phase microstructure after compaction by SPS. Microstructure refining allows to reach values of compressive fracture strength above 300 MPa, while as cast ingots do not exceed 150 MPa. Dimensionless figure of merit ZT is improved with respect to as cast ingots, as a consequence of the increase of Seebeck coefficient, and the decrease of electrical conductivity and thermal conductivity. An alternative approach for increasing mechanical properties of Zn_4Sb_3 consists in developing a composite by dispersion of a second phase with different properties from the matrix [11,12]. An in situ composite can be obtained by adding an excess of Zn with respect to the stoichiometry of the compound [11]. It was observed that an increase of the amount of ductile Zn phase in the composite leads, on the one hand, to an increase of fracture toughness and, on the other hand, to a decrease of power factor. Finally, addition of SiC whiskers to the Zn_4Sb_3 matrix allows to obtain ex situ composite by hot extrusion or hot pressing [12]. Increasing volume fraction of SiC whiskers (up to 5 vol. %), fracture toughness increases, power factor remains constant and thermal conductivity increases, leading to a decrease of ZT.

In conclusion, both thermoelectrical and mechanical properties of Zn_4Sb_3 compound strongly depends on the powder production and on the sintering process. In this work, we investigate the synthesis of Zn_4Sb_3 after compaction by open die pressing [16] using powders produced from slowly cooled ingots and from rapid solidified ribbons. Mechanical and thermoelectric properties are investigated and the results are discussed in terms of structural and microstructural stability.

2. Materials and methods

For master alloy preparation, pure elements (99.999%), sealed in a silica vial under Ar, were annealed in a muffle furnace at 1023 K for 10 h, and subsequently cooled to room temperature in 5 h.

Rapidly solidified samples of Zn_4Sb_3 were obtained in the form of fragmented ribbons with a planar flow casting apparatus (Edmund Bühler GmbH). The master alloy was induction melted in a BN crucible and ejected by an Ar overpressure (0.2 bar) on a copper wheel rotating at 20 m/s. Powders obtained by grinding the master alloy (MA) or the rapidly solidified (RS) ribbons were sintered by open die pressing (ODP) at 558 K for 5 min: the sample obtained were named ODP − MA and ODP − RS, respectively. Prior to sintering, the powders were packed under Ar atmosphere in a Fe sheath internally coated by a BN thick layer, annealed up to 558 K in 10 min and immediately placed between the heated plates of the compression machine. Compaction of the powders was obtained by increasing the load up to 343 kN until a deformation of about 55% (measured by the bar displacement) was obtained, afterwards the load was reduced to 196 kN for the remaining time, in order to maintain the deformation constant.

Metallographic characterization of the samples was performed with an optical microscope (Leica DMLM).

Density of the samples was measured in distilled water with a picnometer.

Inductively Coupled Plasma-Atomic Electronic Spectroscopy (ICP-AES) analysis was used for elemental analysis of the samples.

Structural characterization was performed by X-ray diffraction (XRD) analysis. Measurements were performed on powdered samples using a PANalytical X'Pert Pro diffractometer with Bragg-Brentano geometry and Cu Kα radiation. Lattice parameters and quantitative analysis of the phases were determined by Rietveld refinement of the XRD patterns using MAUD software [17].

A Scanning Electron Microscope (SEM) Leica Steroscan 410 equipped with an Oxford Instruments INCAx-sight probe for Energy Dispersive X-ray analysis (EDX) was used to examine the microstructure and determine phase composition.

Thermal stability of the samples was investigated by differential scanning calorimetry (DSC) with a power compensation Perkin Elmer DSC7 using scanning rates of 4 K/min and 8 K/min upon heating and cooling, respectively.

Seebeck coefficient of the processed samples was measured as a function of the temperature using MMR Technology apparatus between 300 K and 700 K. Average heating and cooling rates were 4 K/min and 8 K/min, respectively.

Room temperature stress-strain tests were performed in compressive mode with a MTS 2/M mechanical test machine with a strain rate of 1.7 10^{-5} s^{-1}.

Microhardness measurements were performed with a Buehler microhardness tester using a load of 4.9 N.

3. Results and discussion

3.1. Microstructure, phase evolution and thermoelectric properties

The optical micrographs of the cross section of MA, ODP − MA and ODP − RS samples (Fig. 1(a), (b) and (c), respectively) show a progressive reduction of residual porosity (dark spots). Conversely, when density is measured with the picnometer (Table 1) the values are similar for all the samples and very close to those reported in the literature (e.g. 6.36 g/cm^3 [2]). This apparent contradiction is due to the presence of open porosity that, on the one hand, is visible by optical observations and, on the other hand, cannot be evaluated by density measurements with the picnometer.

According to ICP-AES analysis (Table 1), the master alloy has a composition very close to the nominal one ($Zn_{57.1}Sb_{42.9}$ at.%), whereas both samples processed by ODP show slight excess of Sb with respect to the master alloy, suggesting a loss of Zn during open die pressing process.

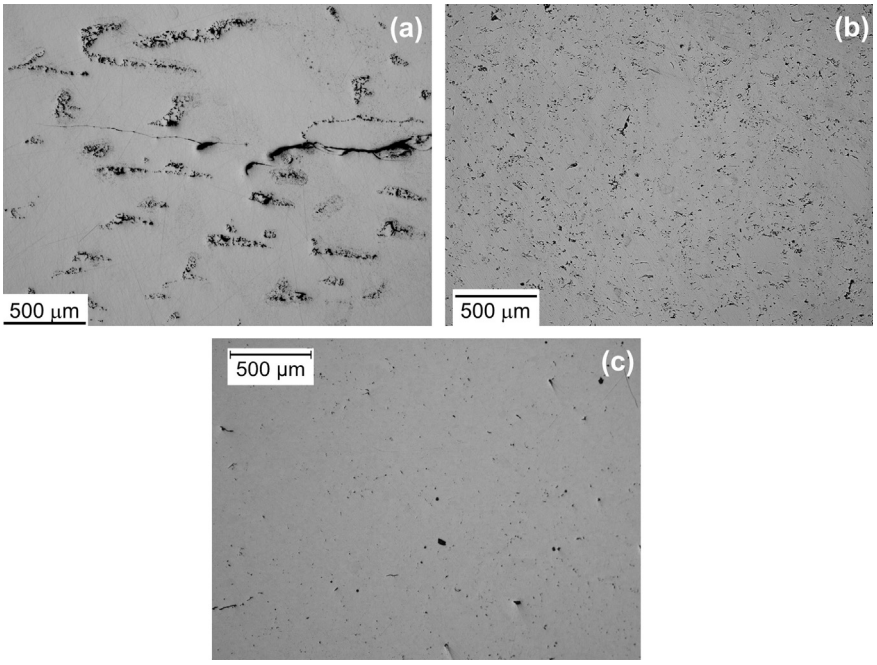

Fig. 1. Optical microscopy images of MA (a), ODP − MA (b) and ODP − RS (c) samples.

Table 1
Chemical composition (standard deviation between 0.1 and 0.4 at.%), density, Vickers hardness, indentation fracture toughness (K_{IC}) and fracture strength (σ_f) for master alloy (MA), ODP − MA and ODP − RS samples.

Sample	Chemical composition		Density (g/cm^3)	Hardness (HVN)	K_{IC} ($MPa\ m^{1/2}$)	σ_f (MPa)
	Zn (at.%)	Sb (at.%)				
Master alloy (MA)	57.3	42.7	6.35	231 ± 4	–	38
ODP − MA	55.6	44.4	6.30	241 ± 10	0.9 ± 0.1	283
ODP − RS	55.9	44.1	6.31	220 ± 18	0.8 ± 0.2	395

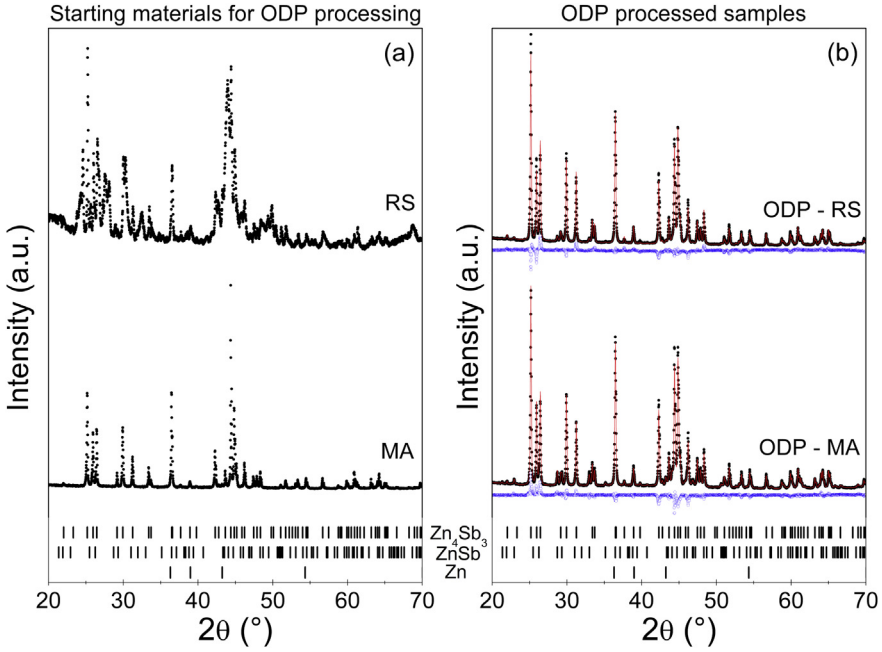

Fig. 2. (a): Experimental X-ray diffraction patterns of the starting materials (MA and RS) used for the subsequent ODP process for sintering. (b): experimental (filled circles) and calculated (continuous line) XRD patterns, together with their difference (open circles), of ODP − MA and ODP − RS sintered samples.

Table 2
Relative quantities of crystalline phases, lattice parameters and R_w obtained by Rietveld refinement of XRD patterns of ODP – MA and ODP – RS samples shown in Fig. 2(b).

Sample	Phase	wt. %	Lattice parameters			R_w (%)
			a (Å)	b (Å)	c (Å)	
ODP – MA	Zn_4Sb_3	Bal.	12.233	12.233	12.430	6.1
	ZnSb	8	6.204	7.738	8.098	
	Zn	<1	2.665	2.665	4.947	
ODP – RS	Zn_4Sb_3	Bal.	12.236	12.236	12.433	6.7
	ZnSb	3	6.207	7.738	8.101	
	Zn	<1	2.665	2.665	4.947	

XRD patterns of the samples obtained at different steps of the process are reported in Fig. 2. Fig. 2(a) shows the XRD patterns of the starting powders used for the subsequent sintering process by ODP. In the case of the master alloy, only Zn_4Sb_3 is present, whereas in rapidly solidified ribbons ZnSb is present beside Zn_4Sb_3, and a broadening of the peaks is observed. As already discussed in Ref. [18], because of the rapid cooling rate, a certain amount of the high temperature ZnSb phase is retained and a highly defective microstructure, eventually including a fraction of amorphous phase, is produced.

In Fig. 2(b) the experimental and the refined patterns (filled circles and continuous lines, respectively) of the ODP processed samples are reported, together with their difference (open circles). Both ODP – MA and ODP – RS samples show the peaks of ZnSb and Zn, together with those of Zn_4Sb_3. The relative amount and the lattice parameters of the various phases are reported in Table 2. ODP – MA sample contains a larger amount of ZnSb and consequently a lower amount of Zn_4Sb_3, with respect to ODP – RS. Pure Zn is barely observable in both samples. Lattice parameters of the phases are consistent with those reported in the literature [19]. The narrow peaks observed in the XRD pattern of the ODP – RS sample indicate that the sintering process, performed above the recrystallization temperature of the alloy (~420 K), turned the highly defective microstructure of the rapidly solidified ribbons into a less defective one.

Fig. 3(a) and (b) show the backscattered SEM image of the as prepared ODP – MA and ODP – RS samples, respectively. The grey matrix corresponds to Zn_4Sb_3, while the bright phase dispersed in the matrix is ZnSb. At high magnification, small dark particle of Zn are visible, as shown in the inset of Fig. 3(a) and (b). All the phases observed are the same detected by XRD (Fig. 2(b) and Table 2).

Fig. 4 shows the effect of thermal cycling between 323 K and 700 K on the DSC traces of the ODP – RS sample as a function of temperature. The as prepared sample shows two consecutive endothermic signals corresponding to the following reactions [20]:

$$LT - \ Zn_4Sb_3 + Zn \rightarrow Zn_3Sb_2 \quad (1)$$

$$Zn_3Sb_2 + Zn \rightarrow liq. \quad (2)$$

As the sample is thermally cycled between 323 K and 700 K, the two signals progressively becomes less intense and disappear after 5 cycles.

After thermal cycling, Zn is no longer present in the ODP – RS sample, as shown by the backscattered SEM image of Fig. 3(c), while some residual ZnSb phase is still present. Upon heating, atomic mobility is favoured leading to the reaction

$$Zn + ZnSb \rightarrow Zn_4Sb_3 \quad (3)$$

with consequent homogenization of the sample.

At each thermal cycle, the amount of Zn available for reactions (1) and (2) is reduced and, consequently, the intensity of the signals related to these two reactions decreases. The disappearance of the two endothermic peaks during the fifth cycle indicates that the whole amount of Zn was consumed by reaction (3). Since the average composition of the sample is richer in Sb with respect to the stoichiometry of the Zn_4Sb_3 compound, the presence of a residual amount of ZnSb is expected, as confirmed by Fig. 3(b).

Fig. 5(a) shows the effect of thermal cycling between 323 K and 700 K on the Seebeck coefficient (α) of the ODP – RS sample. During the first cycle, the temperature dependence of the Seebeck shows a maximum (about 280 μV/K) at 400 K, followed by a continuous decrease. During the second and third cycles, the maximum at about 400 K progressively decreases to ~200 μV/K and 150 μV/K, respectively, and it is followed by a continuous increase with temperature. During the fourth and fifth cycles, the maximum at 400 K disappears and the Seebeck coefficient shows

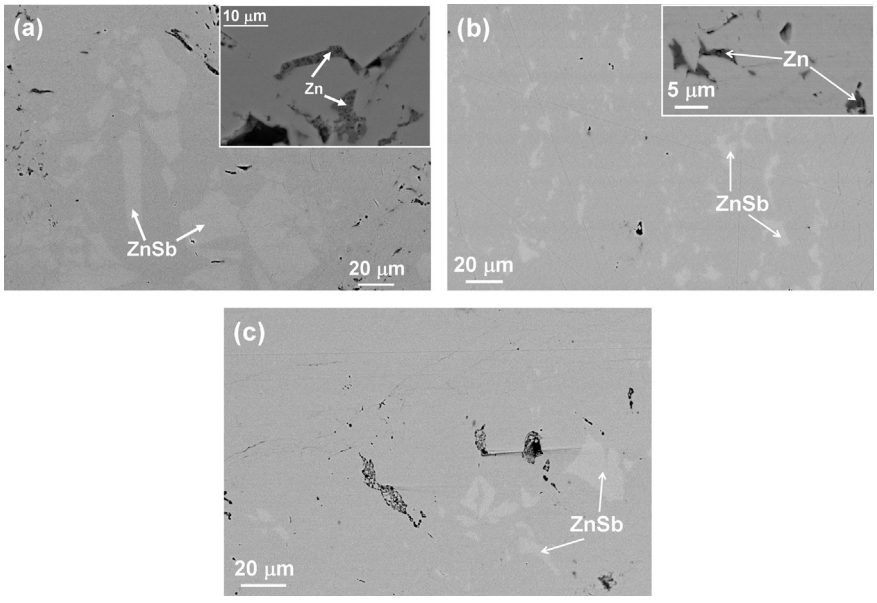

Fig. 3. Backscattered electrons SEM images of the microstructure of ODP – MA (a), ODP – RS before (b) and ODP – RS after (c) thermal cycling.

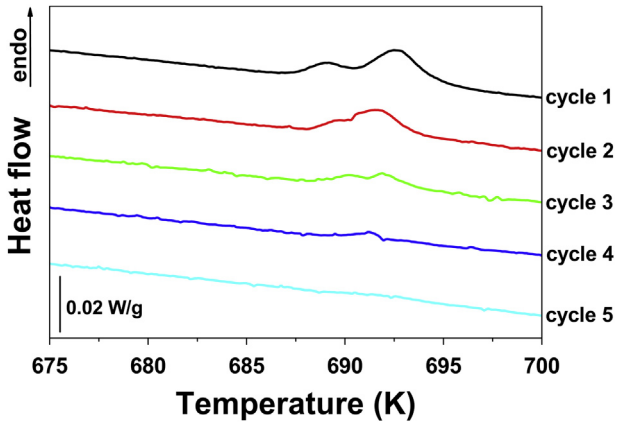

Fig. 4. DSC heating cycles of ODP – RS sample at 4 K/min between room temperature and 700 K.

a reproducible continuous increase with temperature. As shown by XRD analysis, Fig. 2(b) and Table 2, and SEM observations, Fig. 3(a), the as prepared ODP – RS sample contains ZnSb as well as Zn. In multiphase systems, the Seebeck coefficient depends on the thermopower behaviour of the single phases. The Seebeck coefficient of ZnSb ranges from 200 μV/K [21,22] to 400 μV/K [23,24] at room temperature, and its temperature dependence shows a maximum value between 400 K and 500 K [17–20]. In the case of Zn_4Sb_3, α is around 100 μV/K at room temperature

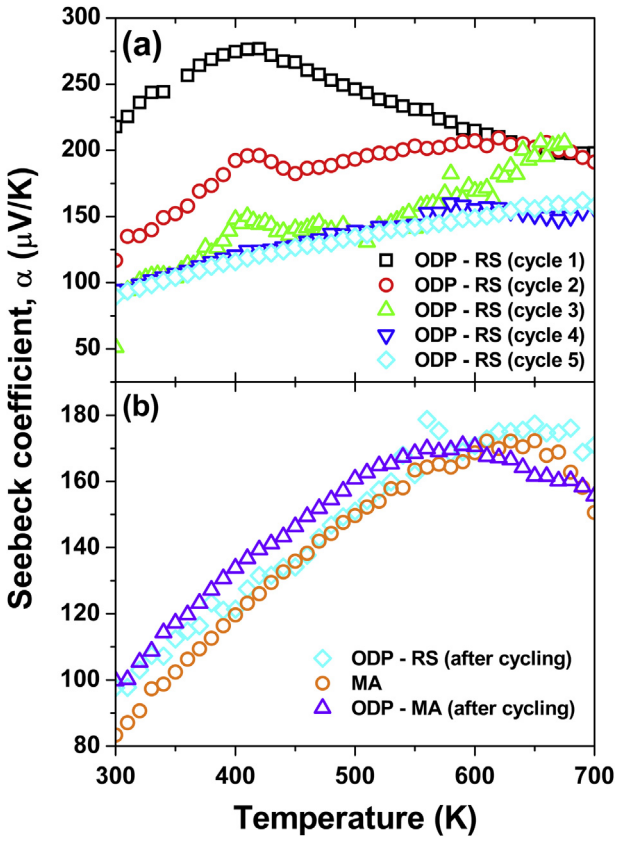

Fig. 5. (a): Effect of thermal cycling between room temperature and 700 K (4 K/min upon heating, 8 K/min upon cooling) on the temperature dependence of Seebeck coefficient for ODP – RS sample. (b): temperature dependence of Seebeck coefficient for as prepared master alloy (empty triangles), ODP – MA sample (open circles) and thermally cycled ODP – RS sample (open diamonds).

and shows a continuous increase with temperature [6]. Thus, in the as prepared ODP – RS sample, the presence of ZnSb is responsible for the enhanced values of α at room temperature with respect to Zn_4Sb_3 single phase, and for the maximum around 400 K. As the sample is progressively homogenized by thermal cycling, the values and the temperature dependence of α tend to become those expected for Zn_4Sb_3 single phase. Both the disappearance of the endothermic peaks in DSC traces between the fourth and the fifth cycles, due to consumption of Zn by reaction (3), and the appearance of a reproducible temperature dependence of the Seebeck coefficient between the fourth and fifth cycles can be correlated to the sample homogenization. A similar behaviour is also observed for the ODP – MA sample (not shown). In this case, seven thermal cycles are needed before observing thermopower reproducibility, because of the larger amount of ZnSb and Zn in ODP – MA sample with respect to ODP – RS sample.

Fig. 5(b) shows the temperature dependence of the Seebeck coefficient for the as prepared master alloy and the thermally cycled ODP – MA and ODP – RS samples. The three samples show qualitatively similar behaviours, and the one observed for MA sample is the reference for the single Zn_4Sb_3 phase. In the low temperature range (between 300 K and 450 K), α(ODP – MA) > α(ODP – RS) > α(MA). In the medium temperature range (between 450 K and 600 K), α(ODP – MA) > α(MA) ≅ α(ODP – RS). In the high temperature range (between 600 K and 700 K), all the samples show a more scattered behaviour of the Seebeck coefficient as a function of temperature and a clear trend cannot be defined. The larger value of α observed for ODP – MA sample in the low and medium temperature range (between 300 K and 600 K) is due to the presence of the residual ZnSb phase after thermal cycling. The temperature dependence of α for the ODP – RS sample can be explained, on the one hand, by the presence of the residual ZnSb phase after thermal cycling, that tends to increase the value of α, and, on the other hand, by the finer dispersion of this phase in the Zn_4Sb_3 matrix with respect to ODP – MA, that leads to a thermopower behaviour that is mainly dominated by the one of Zn_4Sb_3 (i.e. MA sample).

The phase evolution of the starting materials observed upon ODP processing and during the following thermal cycling (i.e. DSC and Seebeck coefficient measurements) can be explained in terms of competing reactions driven by thermodynamics or kinetics [7]. Fig. 6 shows a schematic TTT curve, adapted from Ref. [7], used for describing the decomposition of Zn_4Sb_3 into Zn and ZnSb. According to Lin et al. [7], the decomposition reaction is observed in the range between 425 K and 565 K and it occurs because of weakening Zn–Sb bonds which allows Zn diffusion and subsequent nucleation and growth of Zn and ZnSb precipitates. Below 425 K, the activation energy of Zn diffusion kinetically inhibits the decomposition of Zn_4Sb_3 which is trapped in a metastable state. Above 565 K, the recombination of Zn and ZnSb into Zn_4Sb_3 becomes more favourable with respect to its decomposition and Zn_4Sb_3 is formed, because of its thermodynamic stability.

The dashed line in Fig. 6 represents the processing temperature (558 K) for the ODP sintering of the samples studied in this work. The ODP sintering temperature falls in the temperature window where decomposition of Zn_4Sb_3 is promoted. Since ODP – MA and ODP – RS samples were processed by ODP in the same conditions (i.e. temperature and time), the same degree of decomposition is expected for both samples. However, quantitative analysis of the XRD patterns, Table 2, unexpectedly shows that in ODP – RS sample there was a lower degree of decomposition with respect to ODP – MA sample. This apparent anomaly can be explained by the different free energy level of the starting materials (MA and RS)

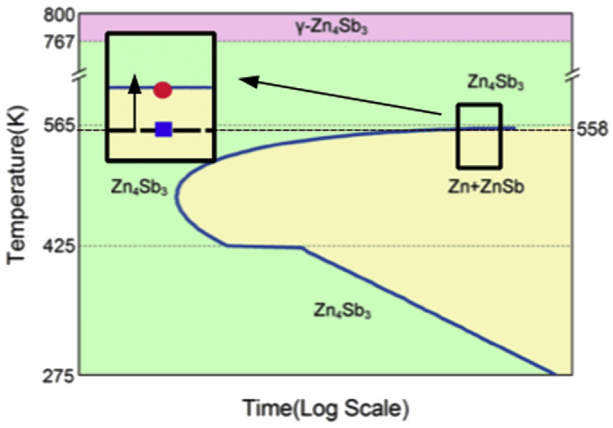

Fig. 6. TTT curve for the decomposition of Zn4Sb3 (adapted from Ref. [7]). Horizontal dashed line represents the processing temperature for ODP sintering. The inset shows the temperature increase of the ODP – RS sample (filled circle) with respect to the ODP – MA (open square) that is related to the different levels of free energy of the starting materials.

used for compaction. On the one hand, ground MA powders are characterized by the presence of only the equilibrium Zn_4Sb_3 phase. In this case, the ODP processing promotes the sintering of the grains and the redistribution of the material following the plastic deformation of the external sheath. On the other hand, the presence of additional phases (ZnSb, amorphous) beside Zn_4Sb_3 indicates that the rapidly solidified ribbons consist of a metastable mixture, with an excess of free energy with respect to the equilibrium. This is confirmed by the irreversible release of heat during DSC scan (exothermic signals between 480 K and 520 K) [18]. Consequently to the release of heat during ODP processing, the ODP – RS sample (filled circles in the inset of Fig. 6) is subject to an increase of temperature that slows down Zn_4Sb_3 decomposition with formation of a lower amount of ZnSb and Zn with respect to ODP – MA sample (filled square in the inset of Fig. 6).

3.2. Mechanical properties

Stress strain tests under compression revealed a typical brittle behaviour with no evidence of plastic deformation. The values of fracture strength (σ_f) for the ODP samples (283–395 MPa) are almost one order of magnitude larger than the value measured for the master alloy (38 MPa), as shown in Table 1. The higher value of σ_f observed in the ODP – RS sample is consistent with its lower porosity and the refined microstructure of the starting melt spun material. A similar result was reported in Ref. [15], where SPS processing of melt spun Zn_4Sb_3 led to a compressive fracture strength above 300 MPa.

Microindentation tests with Vickers pyramid (4.9 N) showed comparable mean hardness values (220–240 HV, Table 1) for all the different samples, irrespectively of the processing route. The values obtained are in agreement with those reported in Ref. [11] (217–233 HVN).

Fig. 7 shows residual Vickers indents (4.9 N) with different cracks patterns on the surface of the ODP – RS sample. Fig. 7(a) shows the presence of both radial and lateral cracks around the indent. Initial chipping of material is visible due to the propagation of lateral cracks on the sample surface. As expected, chipping becomes more evident increasing the indentation load (24.5 N, not shown here). Fig. 7(b) shows well developed radial cracks from the corners of the indent. Fig. 7(c) shows Palmqvist radial cracks after delicate polishing of the indented surface shown in Fig. 7(b). The condition for assessing fracture toughness from residual Vickers indents is the development of symmetric radial cracks and the absence of lateral cracks. In fact, the activation of radial cracks implies that part of the energy is partitioned at expense of the radial crack growth, leading to an overestimation of the indentation fracture toughness [25].

In the case of the MA sample, indentation fracture toughness (K_{IC}) could not be determined, because all the examined residual indents always revealed the presence of lateral cracks. In the case of the ODP – MA sample, most of the indents showed the presence of lateral cracks. Thus, only few indents could be used for the assessment of K_{IC}. Conversely, in the ODP – RS sample, indents with symmetric radial cracks were prevalent.

In presence of Palmqvist radial cracks, Fig. 7(c), indentation fracture toughness can be determined using the following equation [26]:

$$K_{IC} = 0.0089\left(\frac{E}{H}\right)^{2/5} P\left(al^{1/2}\right) \quad (4)$$

where, E is the Young modulus (72 GPa) [11], H is the hardness, P is the indentation load, a is the half diagonal of the indent, l is the length of the radial crack from the indent corner. The mean values of K_{IC} obtained for ODP – MA and ODP – RS samples (0.8–0.9 MPa $m^{1/2}$), Table 1, are in line with those reported in the literature (0.6–1.4 MPa $m^{1/2}$) [9,11], and indicate a behaviour typical of brittle ceramics [27].

ODP – MA and ODP – RS samples show similar values of K_{IC}, suggesting that, when symmetric radial cracks develop without propagation of lateral cracks, the mechanical properties of Zn_4Sb_3 are reproducible, independently of the processing route. However, lateral cracks propagation is affected by the processing route, since it becomes progressively less frequent in MA, ODP – MA and ODP – RS samples. This behaviour can be explained by the progressive reduction of porosity in the samples series. In fact, free surfaces around the pores accommodate residual stress that likely leads to an easier propagation of lateral cracks and, possibly, to chipping.

4. Conclusions

In this work, compact bulk samples of Zn_4Sb_3 were produced by sintering with open die pressing process at 558 K.

Sintering induces, with respect to master alloy ingots, the decrease of porosity, a slight decrease in Zn content and the partial decomposition of Zn_4Sb_3 into ZnSb and Zn. Further decrease of the open porosity and partial inhibition of Zn_4Sb_3 decomposition was achieved by using ground rapidly solidified ribbons, instead of ground slowly cooled master alloy, as a starting material for sintering. As sintered samples show a temperature behaviour of the Seebeck coefficient that is intermediate between those of Zn_4Sb_3 and ZnSb.

Thermal cycling between 300 K and 700 K of the sintered samples induces recombination of ZnSb and Zn into Zn_4Sb_3, with consequent homogenization of the microstructure and recovery of the Seebeck coefficient behaviour typical of Zn_4Sb_3 single phase. The phase evolution observed upon sintering and thermal cycling depends on the free energy level of the starting materials used for sintering.

All the samples show a brittle behaviour upon stress-strain compression tests and microindentation measurements. Fracture strength of the samples increases (from about 40 MPa up to 300–400 MPa) with the decrease of residual porosity. Similar hardness values were obtained for all samples (220–240 HVN). Indents are surrounded by Palmqvist-type radial cracks, however, as residual porosity increases, lateral cracks also appear. Values of

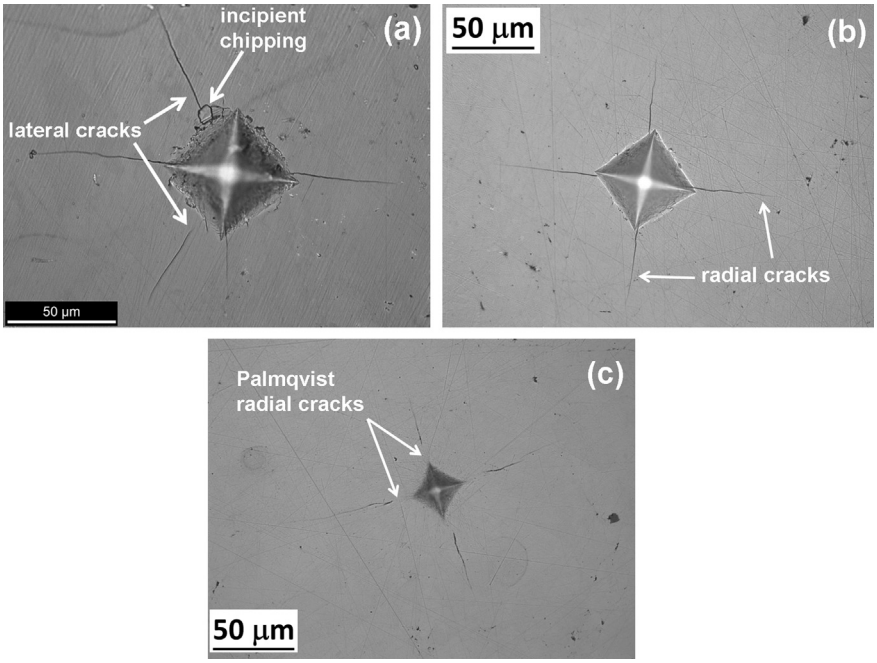

Fig. 7. Residual Vickers indents with different cracks patterns in ODP – RS sample. (a): incipient chipping due to propagation of lateral cracks on the sample surface. (b): development of symmetric radial cracks from the indent corners. (c): Palmqvist radial cracks after light polishing of the indented sample surface shown in Fig. 7(b).

indentation fracture toughness (0.8–0.9 MPa $m^{1/2}$) were estimated for the sintered samples in absence of lateral cracks.

Acknowledgements

The authors wish to thank Enrico Bassani (CNR - Istituto per l'Energetica e le Interfasi, Lecco, Italy) for the ODP processing of the samples and Prof. Gilda Zanicchi (University of Genoa, Italy) for useful discussion of the results.

A. Castellero and M. Baricco acknowledge financial support by Regione Piemonte (DRAPO′ project).

References

[1] S. LeBlanc, Thermoelectric generators: linking material properties and systems engineering for waste heat recovery applications, Sustain. Mater. Technol. 1–2 (2014) 26–35.
[2] G.J. Snyder, M. Christensen, E. Nishibori, T. Caillat, B.B. Iversen, Disordered zinc in Zn_4Sb_3 with phonon-glass and electron-crystal thermoelectric properties, Nat. Mater 3 (2004) 458–463.
[3] B.B. Iversen, Fulfilling thermoelectric promises: β-Zn_4Sb_3 from materials research to power generation, J. Mater. Chem. 20 (2010) 10778–10787.
[4] Y. Mozharivskyj, A.O. Pecharsky, S. Bud'ko, G.J. Miller, A promising thermoelectric material: Zn_4Sb_3 or $Zn_{6-\delta}Sb_5$. Its composition, structure, stability, and polymorphs. Structure and Stability of $Zn_{1-\delta}Sb$, Chem. Mater 16 (2004) 1580–1589.
[5] J.-B. Li, M.-C. Record, J.-C. Tedenac, A thermodynamic assessment of the Sb-Zn system, J. Alloys Compd. 438 (2007) 171–177.
[6] T. Caillat, J.-P. Fleurial, A. Borshchevsky, Preparation and thermoelectric properties of semiconducting Zn_4Sb_3, J. Phys. Chem. Solids 58 (1997) 1119–1125.
[7] J. Lin, X. Li, G. Qiao, Z. Wang, J. Carrete, Y. Ren, L. Ma, Y. Fei, B. Yang, L. Lei, J. Li, Unexpected High-temperature stability of β–Zn_4Sb_3 opens the door to enhanced thermoelectric performance, J. Am. Chem. Soc. 136 (2014) 1497–1504.
[8] B.L. Pedersen, B.B. Iversen, Thermally stable thermoelectric Zn_4Sb_3 by zone melting synthesis, Appl. Phys. Lett. 92 (2008) 161907.
[9] K. Ueno, A. Yamamoto, T. Noguchi, T. Inoue, S. Sodeoka, H. Obara, Optimization of hot-press conditions of Zn4Sb3 for high thermoelectric performance II. Mechanical properties, J. Alloys Compd. 388 (2005) 118–121.
[10] M. Tapiero, S. Tarabichi, J.G. Gies, C. Noguet, J.P. Zielinger, M. Joucla, J.L. Loison, M. Robino, Preparation and characterization of Zn_4Sb_3, Sol. Energy Mat. 12 (1985) 257–274.
[11] S.-C.- Ur, P. Nash, R. Schwarz, Mechanical and thermoelectric properties of Zn4Sb3 and Zn4Sb3+Zn directly synthesized using elemental powders, Metals Mater. Int. 11 (2005) 435–441.
[12] T. Akao, Y. Fujiwara, Y. Tarui, T. Onda, Z.-C. Chen, Fabrication of Zn_4Sb_3 Bulk Thermoelectric Materials Reinforced with SiC Whiskers, J. Electron. Mater 43 (2014) 2047–2052.
[13] K. Ueno, A. Yamamoto, T. Noguchi, T. Inoue, S. Sodeoka, H. Obara, Optimization of hot-press conditions of Zn_4Sb_3 for high thermoelectric performance III. Effect of starting particle size on thermoelectric and mechanical properties, J. Alloys Compd. 392 (2005) 295–299.
[14] T. Souma, G. Nakamoto, M. Kurisu, Low-temperature thermoelectric properties of α- and β- Zn_4Sb_3 bulk crystals prepared by a gradient freeze method and a spark plasma sintering method, J. Alloys Compd. 340 (2002) 275–280.
[15] D. Qi, X. Tang, H. Li, Y. Yan, Q. Zhang, Improved thermoelectric performance and mechanical properties of nanostructured melt-spun β- Zn_4Sb_3, J. Electron. Mater 39 (2010) 1159–1165.
[16] S. Ceresara, C. Fanciulli, F. Passaretti, D. Vasilevskiy, Texturing of $(Bi_{0.2}Sb_{0.8})_2Te_3$ nanopowders by open die pressing, J. Electron. Mater 42 (2013) 1529–1534.
[17] http://www.ing.unitn.it/~maud/index.html.
[18] R. Carlini, A. Castellero, C. Fanciulli, F. Passaretti, M. Baricco, G. Zanicchi, Phase selection and microstructure refinement of melt-spun Zn_4Sb_3-type compound, in: A. Amaldi, F. Tang (Eds.), Proceedings of the 11th European Conference on Thermoelectrics: ECT 2013, Springer International Publishing, Cham (Switzerland), 2014, pp. 29–35.
[19] P. Villars, L.D. Calvert (Eds.), Pearson's Handbook of Crystallographic Data for Intermetallic Phases, vol. 3, American Society for Metals, Metals Park, OH, 1985.
[20] J.B. Li, M.-C. Record, J.-C. Tedenac, A thermodynamic assessment of the Sb–Zn system, J. Alloys Compd. 438 (2007) 171–177.
[21] L.T. Zhang, M. Tsutsui, K. Ito, M. Yamaguchi, Effects of ZnSb and Zn inclusions on the thermoelectric properties of β- Zn_4Sb_3, J. Alloys Compd. 358 (2003) 252–256.
[22] G. Zhu, W. Liu, Y. Lan, G. Joshi, H. wang, G. Chen, Z. Ren, The effect of secondary phase on thermoelectric properties of Zn_4Sb_3 compound, Nanoenergy 2 (2013) 1172–1178.
[23] C. Okamura, T. Ueda, K. Hasezaki, Preparation of single-phase ZnSb thermoelectric materials using a mechanical grinding process, Mater. Trans. 51 (2010) 860–862.
[24] P.H.M. Böttger, G.S. Pomrehn, G.J. Snyder, T.G. Finstad, Doping of p-type ZnSb: single parabolic band model and impurity band conduction, Phys. Status Solidi A 208 (2011) 2753–2759.
[25] R.F. Cook, M.R. Pascucci, W.H. Rhodes, Lateral cracks and microstructural effects in the indentation fracture of yttria, J. Am. Ceram. Soc. 73 (1990) 1873–1878.
[26] C.B. Ponton, R.D. Rawlings, Vickers indentation fracture toughness test. Part 1. Review of literature and formulation of standardised indentation toughness equations, Mater. Sci. Technol. 5 (1989) 865–872.
[27] M.F. Ashby, Materials Selection in Mechanical Design, fourth ed., Butterworth-Heinemann, Oxford, 2011, p. 73.